methods

Plasma membrane asymmetry of lipid organization: fluorescence lifetime microscopy and correlation spectroscopy analysis[S]

Anjali Gupta,* Thomas Korte,† Andreas Herrmann,† and Thorsten Wohland[1,*,§]

Department of Biological Sciences and NUS Centre for Bio-Imaging Sciences* and Department of Chemistry,[§] National University of Singapore, Singapore; and Institute for Biology/Biophysics,[†] Faculty of Life Sciences, Humboldt-Universität zu Berlin, Berlin, Germany

ORCID ID: 0000-0002-0148-4321 (T.W.)

Abstract **A fundamental feature of the eukaryotic cell membrane is the asymmetric arrangement of lipids in its two leaflets. A cell invests significant energy to maintain this asymmetry and uses it to regulate important biological processes, such as apoptosis and vesiculation. The dynamic coupling of the inner or cytoplasmic and outer or exofacial leaflets is a challenging open question in membrane biology. Here, we combined fluorescence lifetime imaging microscopy (FLIM) with imaging total internal reflection fluorescence correlation spectroscopy (ITIR-FCS) to differentiate the dynamics and organization of the two leaflets of live mammalian cells. We characterized the biophysical properties of fluorescent analogs of phosphatidylcholine, sphingomyelin, and phosphatidylserine in the plasma membrane of two mammalian cell lines (CHO-K1 and RBL-2H3). Because of their specific transverse membrane distribution, these probes allowed leaflet-specific investigation of the plasma membrane. We compared the results of the two methods having different temporal and spatial resolution. Fluorescence lifetimes of fluorescent lipid analogs were in ranges characteristic for the liquid ordered phase in the outer leaflet and for the liquid disordered phase in the inner leaflet. The observation of a more fluid inner leaflet was supported by free diffusion in the inner leaflet, with high average diffusion coefficients. The liquid ordered phase in the outer leaflet was accompanied by slower diffusion and diffusion with intermittent transient trapping.** **Our results show that the combination of FLIM and ITIR-FCS with specific fluorescent lipid analogs is a powerful tool for investigating lateral and transbilayer characteristics of plasma membrane in live cell lines.—** Gupta, A., T. Korte, A. Herrmann, and T. Wohland. **Plasma membrane asymmetry of lipid organization: fluorescence lifetime microscopy and correlation spectroscopy analysis.** ***J. Lipid Res.*** **2020.** 61: **252–266.**

Supplementary key words diffusion • liquid order • liquid disorder • membrane phase

The plasma membrane is a bilayer composed of a plethora of chemically diverse lipids and a range of proteins. The distinct physicochemical properties of the membrane components lead to the formation of transient assemblies such as cholesterol-dependent domains, cholesterol-independent domains, and protein oligomers that are typically below the diffraction limit (20–100 nm) and are in dynamic equilibrium with each other (1–3). The transient assemblies exhibit unique life spans governed by the mutual interactions of their components. In addition to the lateral heterogeneity, a fundamental feature of the plasma membrane is the asymmetry of the lipid composition between the two leaflets (4–6). The dynamic lateral heterogeneity of the membrane is essential for cell signaling (7), while the asymmetric arrangement of lipids across the plasma membrane is found to be critical in the regulation of several biological processes, including apoptosis (8), cell-cell fusion (9), and signaling in immune cells (10). The primary classes of lipids that constitute a typical mammalian plasma membrane are glycerophospholipids [e.g., phosphatidylcholine (PC), phosphatidylserine (PS),

This work was supported by a research scholarship from the National University of Singapore (A.G.) and Humboldt-Universität zu Berlin-National University of Singapore Grant R-154-000-A54-133 (H.T.W., A.H.). The authors declare that they have no conflicts of interest with the contents of this article.

Manuscript received 1 September 2019 and in revised form 3 December 2019.

Published, JLR Papers in Press, December 19, 2019
DOI https://doi.org/10.1194/jlr.D119000364

Abbreviations: ACF, autocorrelation function; CCD, charge-coupled device; Chol, cholesterol; DOPC, dioleoyl-*sn*-glycero-3-phosphocholine; FLIM, fluorescence lifetime imaging microscopy; GPMV, giant plasma membrane vesicle; ITIR-FCS, imaging total internal reflection fluorescence correlation spectroscopy; LUV, large unilamellar vesicle; mβcd, methyl-β-cyclodextrin; NBD, 1-palmitoyl-2-[6-[(7-nitro-2-1,3-benzoxadiazol-4-yl)amino]hexanoyl]*sn*-glycero-3-phospholipid; PC, phosphatidylcholine; PS, phosphatidylserine; SSM, *N*-stearoyl-D-sphingomyelin; TF-PC, 1-palmitoyl-2-(dipyrromethaneboron difluoride)undecanoyl-*sn*-glycero-3-phosphocholine; TF-SM, *N*-[11-(dipyrromethaneboron difluoride) undecanoyl]D-erythro-sphingosylphosphorylcholine; 16-doxyl-PC, 1-palmitoyl-2-stearoyl-(16-doxyl)-*sn*-glycero-3-phosphocholine.

[1]To whom correspondence should be addressed.
e-mail: twohland@nus.edu.sg

[S] The online version of this article (available at https://www.jlr.org) contains a supplement.

phosphatidylethanolamine, phosphatidic acid, phosphatidylinositol], sphingolipids (e.g., SMs, ceramides, glycosphingolipids), and cholesterol (11). In the plasma membrane, PC and sphingolipids are prevalent in the outer leaflet, while aminophospholipids such as PS and phosphatidylethanolamine are prevalent in the inner leaflet (4). Because the outer leaflet comprises more domain-forming lipids and the inner leaflet is in direct contact with the cytoskeleton, it is expected that the organization and dynamics of the two leaflets are different. However, the precise lateral and transbilayer organization of the membrane and how the two leaflets are dynamically coupled are unknown. Several studies have focused on understanding the membrane asymmetry and organization; however, due to experimental limitations they have mostly been conducted on model membranes with limited physiological relevance, as it is difficult to recapitulate the structural complexity of an intact cell membrane (12–14). A detailed analysis of plasma membrane asymmetry in a physiological context requires a methodology that can probe the dynamics and organization of both leaflets of an intact cell membrane separately with sufficient spatiotemporal resolution. In addition to the quantitative nature of the method, there are other key points to consider in an analysis of the transbilayer membrane organization (15). First, there should be a way of separating the information originating from the two leaflets. This can be achieved by using lipid probes that confine themselves predominantly to one particular leaflet or by selectively quenching the fluorescence signal from one leaflet using a membrane-impermeable agent such as sodium dithionite, 2,4,6-trinitrobenzenesulfonic acid, or doxyl-PC. Second, the time taken to complete the assay should be less than what it takes for lipids to undergo transbilayer movement. Third, the quenching agent should not have any additional effects on the membrane integrity. Finally, certain chemical treatments can alter the membrane lipid composition by modulating the rates of endo- or exocytosis. Exogenous chemical treatments performed during the analysis of plasma membrane asymmetry should not induce any change in the membrane composition.

We performed a detailed analysis of the plasma membrane asymmetry on the basis of the abovementioned considerations by examining the outer and inner leaflets of the membrane separately in live mammalian cells using a combination of fluorescence lifetime imaging microscopy (FLIM) and imaging total internal reflection fluorescence correlation spectroscopy (ITIR-FCS). FLIM has been utilized to investigate the asymmetrical arrangement of the plasma membrane (16, 17). It can reliably detect and resolve microscopic domains present in model membranes as identified by their different lifetimes. However, in giant plasma membrane vesicles (GPMVs) and intact plasma membranes, where lateral heterogeneities are on the nanometer scale, FLIM cannot resolve discrete membrane domains. Due to the domains, FLIM detects a mixture of lifetimes leading to a broad distribution of fluorescence lifetimes indicating the existence of a wide variety of transient assemblies (16). In order to obtain complementary information to membrane organization as measured by FLIM, we used ITIR-FCS to measure membrane dynamics (18–21). ITIR-FCS is an imaging modality that allows multiplexed FCS measurements on the entire region of interest simultaneously and provides spatially resolved diffusion coefficient and number of particle maps. And although ITIR-FCS is diffraction-limited, the use of the FCS diffusion law, which determines the change of diffusion with spatial scale, allows the investigation of subresolution membrane organization (22, 23). FLIM measurements require environmentally sensitive fluorophores, while for FCS measurements fluorophores with better photostability are ideal. Therefore, we used 1-palmitoyl-2-[6-[(7-nitro-2-1,3-benzoxadiazol-4-yl)amino]hexanoyl]*sn*-glycero-3-phospholipid (NBD)-labeled lipid analogs for FLIM because NBD lifetime is sensitive to the environmental polarity and molecular packing around the probe (17, 24–26) (**Fig. 1A**). However, the low photostability and brightness of NBD make it nonideal for FCS measurements (27). Therefore, we used dipyrrromethene boron difluoride (TopFluor)-labeled lipids, which offer sufficient photostability, for FCS measurements (Fig. 1A). To evaluate cell type, domain, and leaflet-specific information, we examined the biophysical properties of fluorescently labeled PC, SM, and PS analogs in the plasma membrane of CHO-K1 and RBL-2H3 cells. Our FLIM results show that the lifetime of all tested probes was typically longer in the outer leaflet than in the inner leaflet, most convincingly for NBD-PS, which was predominantly localized in the inner leaflet of the membrane. In support of these results, ITIR-FCS measurements on the same cell lines showed a higher diffusion coefficient and less domain-confined diffusion of lipid probes localized in the inner leaflet of the membrane and a slower diffusion accompanied with higher confinement in the outer leaflet of the membrane, with characteristic differences between cell lines. Overall, our results reveal that the outer leaflet exhibits a liquid ordered environment, while the inner leaflet of the membrane is more similar to the liquid disordered phase. Furthermore, we show cell-line differences in the transbilayer organization of the plasma membrane.

EXPERIMENTAL PROCEDURES

Materials and sample preparation

NBD-PC, NBD-SM, NBD-PS, 1-palmitoyl-2-(dipyrromethene boron difluoride)undecanoyl-*sn*-glycero-3-phosphocholine (TF-PC), *N*-[11-(dipyrromethene boron difluoride)undecanoyl]D-erythro-sphingosylphosphorylcholine (TF-SM), 1-palmitoyl-2-(dipyrromethene boron difluoride)undecanoyl-*sn*-glycero-3-phospho-L-serine (TF-PS) (Fig. 1A), and 1-palmitoyl-2-stearoyl-(16-doxyl)-*sn*-glycero-3-phosphocholine (16-doxyl-PC) were purchased from Avanti Polar Lipids (Alabaster, AL). Lipid analogs were solubilized in methanol. Sodium dithionite was purchased from Sigma-Aldrich, Singapore. CHO-K1 and RBL-2H3 cells were purchased from ATCC (Manassas, VA). We used NBD lipid analogs for discerning the microenvironments of the conjugated lipids in CHO-K1 and RBL-2H3 cell membranes by performing FLIM experiments. The fluorescence lifetime of NBD is influenced by the surrounding membrane packing, environmental polarity, and tendency to show red-edge excitation shift.

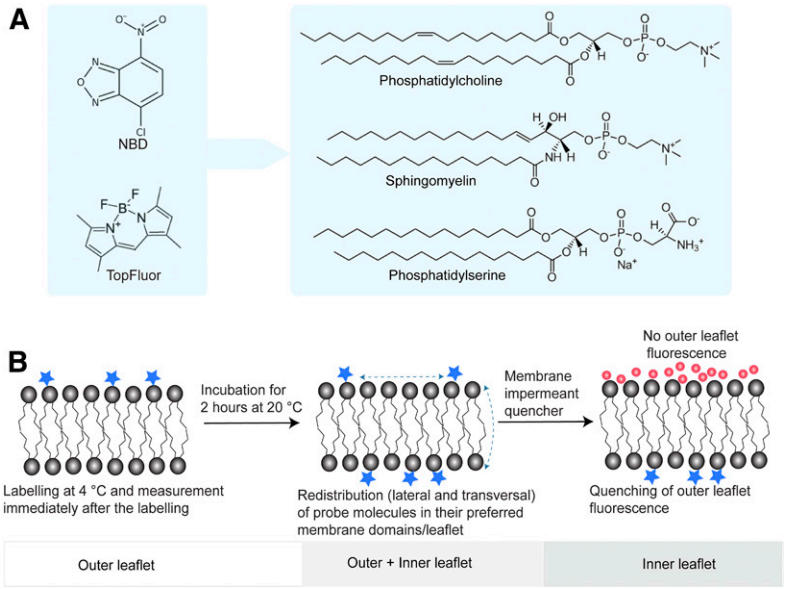

Fig. 1. A: Chemical structures of NBD- and TopFluor-labeled PC, SM, and PS analogs. B: For the readouts from the outer leaflet exclusively, cells are labeled at 4°C and are measured immediately. The probes (lipids marked with asterisks) are then allowed to redistribute in the cell membrane via both lateral and transversal movement, and fluorescence is recorded from probes localized in both the outer and inner leaflets. Finally, outer leaflet probe fluorescence is quenched by treating the labeled cells at 4°C with a membrane-impermeant quencher, as shown by the red circles (NBD: sodium dithionite; TopFluor: 16-doxyl lipids), and then the measurements are performed. Postquenching readouts provide access to inner leaflet organization and dynamics exclusively.

Here, we used TopFluor lipid conjugates for ITIR-FCS measurements because previous reports have demonstrated their compatibility with FCS (28). Sodium dithionite and doxyl-PC were used to quench outer leaflet NBD and TopFluor lipid analogs, respectively. Prior to FLIM measurements on cell membranes, lifetime measurements were performed on large unilamellar vesicles (LUVs) labeled with NBD-PC and TopFluor-PC at temperatures ranging from 25 to 45°C.

Large unilamellar vesicle preparation

LUVs were prepared by evaporating the chloroform from the calculated amounts of lipids and the fluorescent lipid analog in a glass flask under a stream of nitrogen. Dried lipids were resuspended in the buffer solution (150 mM NaCl, 10 mM HEPES, pH 7.4). The solution was then subjected to a freeze-thaw cycle at least eight times to obtain multilamellar vesicles. Finally, the multilamellar vesicle solution was extruded at least 10 times through 100 nm polycarbonate filters (Whatman) at a temperature above lipid-phase separation. For fluorescence lifetime measurements we used 0.2 mM total lipid LUV solutions.

Giant plasma membrane vesicle preparation

GPMVs were prepared from CHO-K1 and RBL-2H3 cells by the formaldehyde-based induction of plasma membrane blebbing. The detailed protocol has been described previously (29). Briefly, cells were grown to ~80% confluency. They were then washed with the vesiculation buffer (10 mM HEPES, 150 mM NaCl, 2 mM $CaCl_2$, pH 7.4). Subsequently, 2 mM DTT and 25 mM PFA were added to the cells followed by an incubation of at least 4 h at 37°C. During this incubation, cells underwent vesiculation to produce GPMVs.

Cell membrane labeling

The stock of both NBD and TopFluor lipid analogs (PC, SM, and PS) (Avanti Polar Lipids) was prepared in pure methanol. For cell membrane staining with NBD lipid analogs, stock solution was diluted in HBSS (Invitrogen, Singapore) to a final concentration of 4 µM. The diluted solution was added to the cells followed by an incubation for 20 min on ice. After incubation, the cells were washed with HBSS at least three times and then used for FLIM experiments. For cell membrane staining with TopFluor lipid analogs, the stock solution was vigorously vortexed and then diluted in HBSS to a final concentration of 5 µM for CHO-K1 cells and 2 µM for RBL-2H3 cells. BSA (3 mg/ml; Sigma Aldrich) was added to the working solution of the fluorescent lipid analogs. The cells were incubated with the working solution (lipid analog-BSA) at 4°C for 15–20 min. After incubation, the cells were washed with DMEM without phenol red (Invitrogen) and 10% FBS at least three times and then the cells were used for imaging.

Preparation of quenching solutions for NBD- and TopFluor-conjugated lipid probes

The outer leaflet fluorescence of NBD and TopFluor was quenched by sodium dithionite and 16-doxyl-PC, respectively. A stock solution of 1 M sodium dithionite was prepared. The stock solution was then diluted to a concentration of 25 mM in 10 mM Tris (pH 9) and used as the working solution. 16-Doxyl-PC was solubilized in pure methanol. The calculated amount of 16-doxyl-PC was added to HBSS to a final concentration of 16 µM.

Determination of the percentage of fluorescent lipid analogs present in the outer leaflet using fluorescence spectroscopy

The fraction of fluorescent lipid analogs was evaluated by quenching outer leaflet fluorescence selectively using cell-impermeant fluorescence quenchers. A cell suspension of about 10^6 cells was centrifuged at 1,000 rpm for 5 min. The pelleted cells were then suspended in the working solution of fluorescent lipid analogs and incubated for 15 min. Cells were again pelleted by centrifugation and resuspended in HBSS. For the redistribution of lipid probes, cells were incubated at room temperature for 2 h. The fluorescence intensity of these cells was measured (excitation at 470 nm) on the Cary Eclipse Fluorescence Spectrophotometer (Singapore). The cells were then pelleted down, and HBSS was replaced with the quenching solution. Cells were suspended in a cold quenching solution and incubated on ice for 10 min. Cold conditions prevent the permeability of quencher inside the cell. The cells were washed with HBSS at least thrice and used for fluorescence intensity measurements.

Cell viability test using trypan blue staining and MTT assay

Cells were labeled with NBD and TopFluor lipid analogs as described above. The cells were then detached with trypsin-EDTA. Cell suspensions were mixed with trypan blue 0.4% solution (Sigma-Aldrich) in a 1:1 ratio, and the percentage of live cells was calculated using a TC20 automated cell counter (BioRad).

Following the cell staining with lipid analogs, cells were incubated at room temperature for 4 h before the measurements.

For the MTT assay, 10^3 cells were seeded in a 96-well plate. After the overnight incubation period, 10 µl (final concentration: 0.5 mg/ml) of the MTT labeling reagent (Sigma-Aldrich) was added to each well. The microplate was incubated for 4 h at 37°C in a humidified incubator. A solubilization solution (100 µl) was then added into the each well. The plate was incubated overnight at 37°C in a humidified incubator, and then the absorbance of the samples was measured at 550 nm and 600 nm using a microplate (ELISA) reader.

Cholesterol depletion experiment

Cholesterol depletion was performed by treating the cells with 3 mM methyl-β-cyclodextrin (Sigma-Aldrich). The cells were incubated with methyl-β-cyclodextrin solubilized in imaging media for 30 min and then measured without washing in between.

Fluorescence lifetime spectroscopy

FLS was performed on a FluoTime 200 spectrometer (PicoQuant, Germany). A pulsed laser diode (LDH-P-C; PicoQuant) of 470 nm and a pulse frequency of 8 MHz were used as the excitation source for NBD probes. Individual photons were recorded on a time-correlated single photon counting setup with a time resolution of 33 ps. NBD emission was recorded at 540 nm, and the spectral bandwidth was set to 4 nm. Mean photon count rates were kept at ~1–4 × 10^4 counts/s. The instrument response function was recorded using HEPES-buffered saline at excitation wavelength. Intensity decays were fitted globally (over at least seven data sets) using a nonlinear least-squares iterative reconvolution fitting procedure (FluoFit; PicoQuant):

$$I(t) = \int_{-\infty}^{t} IRF(t')\left(\sum_{i=1}^{n} \alpha_i e^{\frac{t-t'}{\tau_i}}\right)dt'$$

where $I(t)$ is the fluorescence intensity at time t and α_i is the preexponential factor representing the intensity of the time-resolved decay of the component with lifetime τ_i. All intensity decays were fitted to bi- or triexponential model functions depending on the studied sample. We ensured the quality of fit by the χ^2 value, the distribution of residuals, and the autocorrelation function of residuals. The fitting error was calculated using a support plane error analysis and included in the error estimation.

Fluorescence lifetime imaging microscopy

Instrumentation and data acquisition. Images were acquired with a confocal laser-scanning microscope with an inverted Fluoview 1000 microscope (Olympus, Tokyo, Japan) and a 60× (NA 1.35) oil-immersion objective at 25°C. The frame size of the acquired images was 512 × 512 pixels. For images of cells labeled with NBD fluorescent analogs, the fluorophores were excited with a 488 nm argon ion laser, and the signal was recorded between 500 and 530 nm. We used a commercial FLIM upgrade kit (PicoQuant) to record FLIM measurements. For these measurements, NBD was excited with a pulsed diode laser (pulse width: 60 ps; pulse frequency: 10 MHz; 4 µs/pixel) with a wavelength of 483 nm. Emission light was filtered using a 540/40 bandpass filter, and then single photons were registered with a single photon avalanche photo diode.

For each FLIM measurement, 50–70 frames were recorded; the average photon count rate was kept at ~2–4 × 10^4 counts/s. The images were pseudocolor-coded in accordance with the average lifetime (τ_{av}) of the pixels.

$$\tau_{av} = \frac{\sum_i \alpha_i \tau_i^2}{\sum_i \alpha_i \tau_i}$$

Data analysis. For extracting the fluorescence lifetimes of NBD analogs, membrane regions were selected by applying an intensity threshold to exclude fluorescence from the background or cytoplasm. The selection was further refined manually to exclude regions not associated with the membrane. The overall fluorescence decay curve was then calculated by adding the photons registered from the selected region. The part of the decay curve that comprises instrument response function was removed, and the rest was used for the analysis. A nonlinear least-squares iterative fitting procedure was used to fit the fluorescence decay curves as a sum of exponential terms:

$$F(t) = \sum_i \alpha_i \exp\left(-\frac{t}{\tau_i}\right)$$

where $F(t)$ denotes the fluorescence intensity at time t and α_i denotes a preexponential factor representing the intensity of the time-resolved decay of the component with lifetime τ_i. The quality of fits was evaluated by the distribution of the residuals and the χ^2 value.

A typical FLIM experiment yields a spatial distribution of lifetime (usually lifetime is mapped in a color-coded fashion); however, because the size of membrane domains is below the spatial resolution individual images do not provide any additional insights. Thus, we represent the data in the form of lifetimes and amplitude averaged over the entire membrane.

ITIR-FCS

The ITIR-FCS experiments were done on TopFluor-labeled cell membranes. The experiments were performed at 25°C with 5% CO_2. ITIR-FCS measurements were conducted on an objective-type TIRF microscope (IX-71; Olympus). We used a high-NA oil-immersion objective (PlanApo; 100×, NA 1.45; Olympus), and the sample was excited using a 488 nm laser (Spectra-Physics Lasers, Mountain View, CA), which was then directed into the microscope by a combination of two tilting mirrors. The laser power used for all experiments was between 0.8 and 1 mW. The light was reflected by a dichroic mirror (Z488/532RPC; Semrock) and focused on the objective back focal plane. The incident angle of the light was controlled by the same combination of the tilting mirror, and it was total internally reflected at the glass-water interface. Finally, the light was filtered by the emission filter and detected on the charge-coupled device (CCD) chip of a cooled (−80°C), back-illuminated electron-multiplying CCD camera (iXON 860; 128 × 128 pixels; Andor). Data acquisition was performed using Andor Solis software versions 4.18.30004.0 and 4.24.30004.0. The pixel side length of the CCD chip in the device was 24 µm, corresponding to a pixel side length of 240 nm in the sample plane. For data acquired in the kinetic mode and to reduce the baseline fluctuations, the baseline clamp was switched on. The readout speed was 10 MHz, with a 4.7× maximum analog-to-digital gain and 25 µs vertical shift speed. An electron-multiplying gain of 300 was used for all ITIR-FCS experiments.

The fluorescence intensity signal was recorded from a 21 × 21 pixel region of interest simultaneously as a stack of 30,000–50,000 frames with a 2 ms time resolution. The data were saved as a 16 bit TIFF file. The fluctuations contained in the temporal intensity trace from each pixel were autocorrelated using a multi-tau correlation scheme, and FIJI plug-in ImFCS version 1.49, a home-written

software that is provided at https://www.dbs.nus.edu.sg/lab/BFL/imfcs_image_j_plugin.html, was used to obtain autocorrelation functions (ACFs) (30). Bleach correction was applied on the data using a fourth-order polynomial function. The ACF for each pixel was individually fitted with the following one-particle model for diffusion using the same software.

$$G(\tau) = \frac{1}{N}\left[\mathrm{erf}(p(\tau)) + \frac{1}{p(\tau)\sqrt{\pi}}\left(e^{-(p(\tau))^2} - 1\right)\right]^2 + G_\infty;\ \ p(\tau) = \frac{a}{2\sqrt{D\tau + \sigma^2}}$$

Here, $G(\tau)$ represents the ACF as a function of correlation time (τ), and N, a, D, and σ are the number of particles per pixel, pixel side length, diffusion coefficient, and SD of the Gaussian approximation of the microscope point spread function, respectively. G_∞ represents the convergence value of the ACF at long correlation times.

Fitting of experimentally obtained ACFs with theoretical models yields D and N. Because it is an imaging-based FCS modality, we obtained a spatially resolved diffusion coefficient (D) and the number of particle (N) maps (30). In this study, the data are represented as means ± SDs. The SDs were obtained from the measurements over 441 pixels per experiment. The SD of an ITIR-FCS measurement contains contributions not only from the measurement variability but also from the cell membrane heterogeneity. Each data point for the diffusion coefficient obtained using ITIR-FCS is an average of 441 measurements; therefore, N = 5,292 at least.

Imaging FCS diffusion laws

For analyzing the cell membrane organization below the diffraction limit, we combined ITIR-FCS with FCS diffusion laws. These laws allow probing the mode of molecular diffusion to determine whether the diffusion is free or hindered by trapping sites such as domains (22, 23). To achieve this, we plotted the spatial dependence of the diffusion time of the probe molecules on the observation area size. These plots were then fitted to an SEM-weighted straight line that is mathematically expressed as

$$\tau_d(A_{eff}) = \tau_0 + \frac{A_{eff}}{D}$$

where τ_0 represents the FCS diffusion law intercept. For deriving subresolution information, the diffusion law plot is extrapolated to zero, and the y-intercept (τ_0) is used as an indicator of membrane organization. For a freely diffusing particle, the diffusion time scales linearly with the observation area, and the y-intercept is zero. In the case of domain entrapment and hop diffusion, the relationship between the diffusion time of the molecules and the observation area becomes nonlinear, and the obtained y-intercept is positive and negative, respectively. To perform FCS diffusion law analysis, the data acquired in an ITIR-FCS experiment are utilized. Postacquisition pixel binning (1 × 1 to 5 × 5) followed by convolution with the point spread function of the microscope system generates variable observation areas (A_{eff}). The typical margin of error on the cell membrane is ±0.1, and thus intercepts that lie in this range are indistinguishable for free diffusion. Only intercepts greater than 0.1 can be attributed to domain entrapment in our setup.

RESULTS AND DISCUSSION

We investigated the dynamics and organization of the outer and inner leaflets in the plasma membrane of mammalian cells. For outer leaflet membrane dynamics, we performed measurements at room temperature immediately after labeling cells with fluorescent lipid analogs at 4°C. Both FLIM and ITIR-FCS measurements are done at room temperature within the first 1–5 min after staining. As this is less than the time needed for the transbilayer movement of glycerophospholipids, which typically ranges from several minutes to hours at 37°C (31), measured values report essentially on the outer leaflet. Labeling of cells with fluorescent lipid analogs showed no significant effect on the cell morphology and cell viability as quantified by trypan blue staining and the MTT assay (supplemental Fig. S1). Subsequently, we measured after an incubation of 2 h at room temperature. During this time, lipid analogs redistribute to their preferred locations in the membrane (32, 33). Aminophospholipids (e.g., PS) are recognized by ATP-dependent flippases and are rapidly translocated to the inner leaflet of the membrane (34). In addition, smaller percentages of choline lipids are also translocated to the inner leaflet via passive diffusion. At this stage, we obtain a combined readout of both the outer and inner leaflets. Finally, for the exclusive measurement of inner leaflet dynamics and organization, outer leaflet fluorescence is quenched. The selective quenching of outer leaflet fluorescence is achieved by treating labeled cells by a suitable membrane-impermeable quencher at 4°C (Fig. 1B). NBD lipid analogs are reduced to the nonfluorescent product 7-amino-2,1,3-benzoxadiazol-4-yl by treating the labeled cells with sodium dithionite, and TopFluor lipid analogs are quenched by spin-labeled 16-doxyl-PC (28, 32, 33). Because 16-doxyl-PC incorporates into the outer leaflet of the membrane to quench the TopFluor probe molecules, it might influence the dynamics in the inner leaflet. To examine the effect of doxyl-PC on inner leaflet lipid dynamics, we measured the diffusion of PMT-GFP, a known inner leaflet marker in the presence and absence of doxyl-PC (35, 36). We observed no significant change in the dynamics and organization of PMT-GFP upon doxyl-PC treatment (supplemental Fig. S2). The quenching efficiency was quantified for each fluorescent lipid analog in both CHO-K1 and RBL-2H3 cell membranes (supplemental Table S1).

FLIM measures the fluorescence lifetimes and their fraction, which report on the packing in the probe microenvironment and the prevalence of molecules in different environments, respectively. In an ITIR-FCS experiment, membrane dynamics is characterized by the diffusion coefficient D and membrane organization by the FCS diffusion law intercept τ_0. We use the diffusion coefficient as a readout of molecular mobility of the probe molecules residing in the membrane, and it is likely to increase with a decrease in the membrane domain fraction. The FCS diffusion law intercept (see Experimental Procedures) provides information about the mode of probe organization in the membrane estimated by plotting the dependence of diffusion time over observation area size (22, 23). For a freely diffusing particle, the diffusion law intercept lies in the range of $-0.1\ s < \tau_0 < 0.1s$. A positive intercept ($\tau_0 > 0.1s$) represents transient entrapment of the probe (e.g., in cholesterol sphingomyelin complexes), and a negative intercept ($\tau_0 < -0.1s$) implies a meshwork organization and hop diffusion of probe molecules (e.g., molecules

hindered by the cytoskeleton). In situations in which a molecule is transiently trapped and hindered by a meshwork simultaneously, the intercept represents a weighted average of both diffusion modes (37). In this case, additional measurements that influence either one of the diffusion modes are necessary to disentangle the contributions by hop diffusion and transient trapping.

The fluorescence lifetime of NBD-PC and TopFluor-PC in membranes with discrete domains

First we determined the NBD lifetime within different membrane phases by measuring the lifetime of NBD-PC in LUVs with defined lipid compositions and known phase behaviors (38, 39). The measurements were performed at temperatures ranging from 25 to 45°C. 1,2-Dioleoyl-*sn*-glycero-3-phosphocholine (DOPC)/*N*-stearoyl-D-sphingomyelin (SSM)/cholesterol (Chol) LUVs with molar ratios of 2:2:6 and 1:1:1 form a pure liquid ordered (l_o) phase or coexisting l_d and l_o phases, respectively. For a pure liquid disordered (l_d) phase, DOPC LUVs are used. The fluorescence decay of NBD in LUVs exhibiting a single phase is best fitted to a biexponential model (supplemental Fig. S3). Past studies have suggested that only the long lifetime is sensitive to the membrane environment, while the short lifetime is not dependent on the membrane phase (16, 24). Lifetime data from LUVs with coexisting phases is best fitted to a triexponential model in which the two long lifetimes represent the two membrane phases (l_d and l_o), and the third, the short component, is not sensitive to membrane phases. The information about the lifetime of NBD in discrete domains with known phases provides an expected range of lifetime in the membrane environment and aids in better interpretation of cell membrane data. Because our cell membrane experiments were performed at 25°C, it is important to take a closer look at the lifetimes originating from the two extreme phases (i.e., l_o and l_d phases) at this temperature. At 25°C, NBD lifetime in the l_d phase, that is, in pure DOPC LUVs, is 6.80 ± 0.04 ns; in the l_o phase, that is, in DOPC/SSM/Chol (2:2:6) LUVs, NBD lifetime is 9.94 ± 0.05 ns. LUVs with coexisting domains, that is, DOPC/SSM/Chol (1:1:1), show two membrane environment-sensitive lifetimes: 9.62 ± 0.2 ns in the l_o phase and 5.06 ± 0.3 ns in the l_d phase.

Ideally, the same fluorescent lipid probes should be used for better comparisons. Therefore, we also probed the sensitivity of TopFluor-PC lifetime to the membrane phase (supplemental Fig. S3G–L). In these experiments, we observed that although the lifetime of TopFluor-PC is ~1 ns longer in LUVs exhibiting the l_o phase compared with that in LUVs exhibiting the l_d phase, the dependence of lifetime on the temperature was not very prominent, as there was a change of only 0.2–0.7 ns, which is in the order of the standard deviation. Moreover, the fluorescence decay of TopFluor-PC in LUVs with coexisting phases did not yield phase-specific results. Therefore, TopFluor lipid probes were not suitable for FLIM experiments. For a detailed description of the obtained results, refer to the supplemental information online.

In the next sections, we present the domain- and leaflet-specific dynamics and organization of fluorescent lipid analogs in CHO-K1 and RBL-2H3 cell membranes, which are known to manifest distinct membrane properties and composition (40, 41).

Leaflet-specific analysis of PC fluorescent analogs in CHO-K1 and RBL-2H3 cell membranes

PC is the most abundant lipid in most mammalian membranes. The molecular geometry of PC is cylindrical, and it has the capability of self-organizing as a bilayer. Most PC molecules present in cell membranes are fluid at room temperature (11). More than 50% of the PC lipid analogs reside in the outer leaflet of the plasma membrane as observed by the estimated quenching efficiency (supplemental Table S1). The analysis of NBD-PC fluorescence lifetimes in the outer leaflet of CHO-K1 and RBL-2H3 cells reveal a lifetime of about 10 ns in both cell lines (**Fig. 2A**, B, **Fig. 3A**–H) along with the percentage fraction of long lifetime component ranging from 40% to 55%. By comparing the NBD-PC lifetime obtained in cell membranes with that obtained in LUVs, it is evident that the outer leaflet of both plasma membranes contains a fraction of l_o-phase domains. Using the same experimental conditions, ITIR-FCS measurements on TF-PC show a 2-fold faster *D* (Figs. 2C, D, 3I–N) in CHO-K1 cells ($D = 0.55 \pm 0.15$ μm^2/s) compared with RBL-2H3 cells ($D = 0.24 \pm 0.03$ μm^2/s). These measurements also reveal a transient entrapment as indicated by a positive τ_0 for this probe in both cell lines, with RBL-2H3 cells (τ_0 =1.48 ± 0.23 s) showing a higher value than CHO-K1 cells ($\tau_0 = 0.78 \pm 0.27$ s). Labeled cells were then measured again after the redistribution of probes between both membrane leaflets (see Fig. 1B, middle). These results contain information averaged over both leaflets. Due to technical limitations, the leaflet-specific lipid composition is difficult to analyze in cell membranes. However, it has been reported that the asymmetric distribution of PC differs across cell lines (42). FLIM analysis of NBD-PC-labeled cells postredistribution reveals no significant changes in the probe lifetime, as it remains ~10 ns (*t*-test; $P > 0.05$). However, ITIR-FCS demonstrates a 30% to 40% higher *D* in both cell lines and a lower τ_0 (CHO-K1: 0.78 ± 0.27 to 0.64 ± 0.41 s; RBL-2H3: 1.48 ± 0.23 to 1.14 ± 0.17 s), indicating differences in the inner leaflet organization of both the cell types. Thus, for a clearer understanding of the inner leaflet organization, we measured the biophysical properties of this probe exclusively on the inner leaflet of both cell lines by quenching fluorescent lipids in the outer leaflet. In this case, FLIM revealed a 2 ns reduction in the longest lifetime component compared with that measured on the outer leaflet. With reference to the LUV data (supplemental Fig. S3), this suggests that the inner leaflet resembles an l_d phase. This is supported by the ITIR-FCS results that show a lower *D* in the outer leaflet relative to the inner leaflet (CHO-K1: 0.55–1.11 μm^2/s; RBL-2H3: 0.24 ± 0.03 to 0.43 ± 0.25 μm^2/s) and concurrent drop in τ_0 (CHO-K1: 0.78 ± 0.27 to 0.25 ± 0.06 s; RBL-2H3: 1.48 ± 0.23 to 0.85 ± 0.22 s). As reflected by a higher *D* and lower τ_0 in both cell lines, these results indicate that the liquid ordered domain

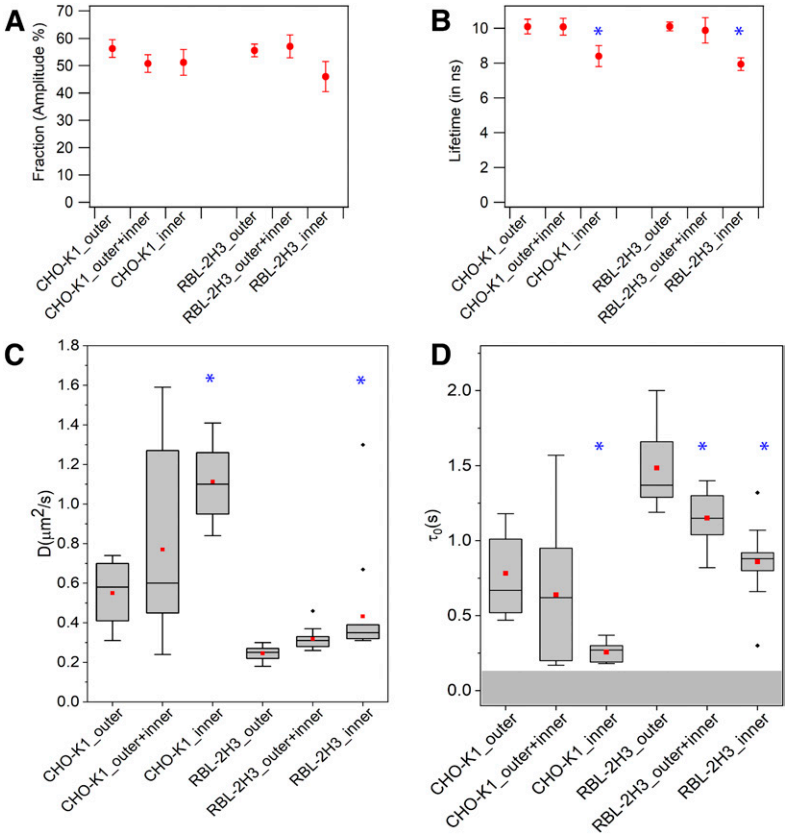

Fig. 2. Leaflet-specific FLIM and ITIR-FCS analysis of fluorescently labeled PC analogs in CHO-K1 and RBL-2H3 cells at room temperature. A: Fraction percentage (amplitude) of NBD-PC long lifetime. B: Long lifetime of NBD-PC measured in nanoseconds. Because out of the three lifetimes obtained for each measurement only the two longer lifetimes are sensitive to the membrane packing, for clarity we show only the long component. C: Average diffusion coefficient of TopFluor-PC. D: FCS diffusion law intercept of TopFluor-PC. Data are pooled averages, and error bars are SDs. ITIR-FCS data are represented as means of boxplots. Maximum and minimum values are shown as vertical boxes with error bars; the 1st and 99th percentiles are shown. Means are shown as red squares. To ensure reproducibility, FLIM experiments were repeated at least three times independently. ITIR-FCS data are the average of at least 12 measurements, each done on different cells from three independent experiments. *Significant differences with respect to the values measured in the outer leaflet (paired *t*-test; $P < 0.05$).

fraction is lower in the inner leaflet. Moreover, a comparison of the two cell lines reveals that the domain fraction is more elevated in RBL-2H3 than CHO-K1 inner leaflets.

The higher domain fraction in RBL-2H3 cells compared with CHO-K1 cells has been addressed in our previous studies (40, 41). Lower lipid mobility and a more significant entrapment of the probe can be attributed to higher levels of sphingolipids in the RBL-2H3 plasma membrane, which is known to form trapping sites in the cell membrane (43).

For additional evidence to support that the more ordered environment in RBL-2H3 cell membranes is due to the plasma membrane lipid composition, we performed FLIM measurements on GPMVs derived from both cell lines. GPMVs were labeled with each of the three NBD analogs. For all NBD probes, we obtained a single peak in the lifetime histogram with average lifetimes around 2 ns shorter than those on cell membranes, consistent with previous reports (44). Below 25°C, GPMVs can show phase separation, but the resulting lifetime histogram remains the same; that is, a single lifetime peak is seen in vesicles with and without phase separation (supplemental Fig. S5C–H). As suggested in previous reports, a single peak in the lifetime histogram in GPMVs is an indication of the presence of a wide variety of lipid domains with relatively similar physicochemical properties (26). A comparison of the lifetimes of probes in the two cell lines revealed an overall longer lifetime of NBD lipid analogs in GPMVs derived from RBL-2H3 cells than CHO-K1 cells (supplemental Fig. S5) measured at 25°C and 37°C. Because GPMVs preserve membrane composition but not organization (29), the long lifetime in RBL-2H3 GPMVs shows that the RBL-2H3 cell membrane composition confers a more ordered environment and a higher domain fraction, supporting both FLIM and FCS results.

Leaflet-specific analysis of SM fluorescent analogs in CHO-K1 and RBL-2H3 cell membranes

The existence of cholesterol-SM complexes in cell membranes has been demonstrated previously (45–47). It is expected that the organization and dynamics of the molecules forming these nanoscale assemblies would differ from those of PC, which is ubiquitously present in the cell membrane. To understand the asymmetric transbilayer organization of domain-specific molecules, we characterized the environment and dynamics of SM fluorescent lipid analogs. SMs are the most abundant sphingolipids present in the plasma membrane of mammalian cells (11).

SMs consist of a ceramide backbone and phosphocholine head group exhibiting a narrower cylindrical geometry than PC and a phase transition above room temperature and thus exist in the gel phase at room temperature. SMs interact with cholesterol to form lipid domains in the membranes but can also exist freely (45, 48, 49). They are predominantly present in the outer leaflet; however, there is some evidence suggesting a pool of SMs localized in the inner leaflet (50, 51). Overall, this is consistent with our quenching experiments that show ~80% of SM lipid analogs are present in the outer leaflet (supplemental Table S1).

The use of tail-labeled NBD lipid analogs for membrane studies is debatable, as they may not behave like the endogenous lipids (52, 53). Therefore, to validate that the NBD

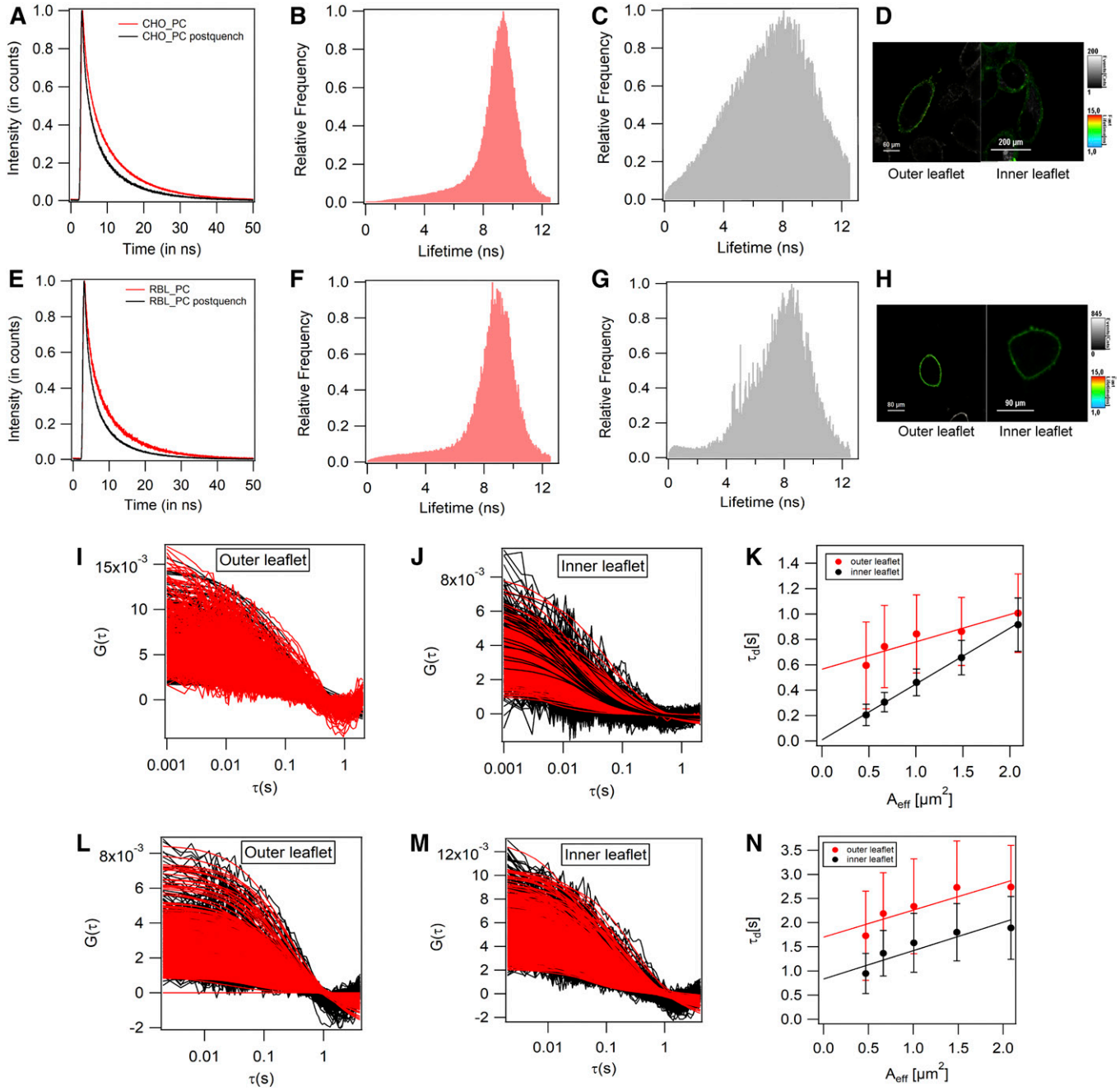

Fig. 3. Representative raw data for FLIM and ITIR-FCS experiments for analyzing leaflet-specific dynamics and organization of PC fluorescent analogs. A: Normalized averaged intensity decay of NBD-PC in the outer and inner leaflets of CHO-K1 cell membranes. B: Normalized lifetime histogram of NBD-PC in the outer leaflet of CHO-K1 cell membranes. C: Normalized lifetime histogram of NBD-PC in the inner leaflet of CHO-K1 cell membranes. D: Lifetime map of CHO-K1 cells labeled with NBD-PC. E: Normalized averaged intensity decay of NBD-PC in the outer and inner leaflet of RBL-2H3 cell membranes. F: Normalized lifetime histogram of NBD-PC in the outer leaflet of RBL-2H3 cell membranes. G: Normalized lifetime histogram of NBD-PC in the inner leaflet of RBL-2H3 cell membranes. H: Lifetime map of RBL-2H3 cells labeled with NBD-PC. I: Autocorrelation curves for TopFluor-PC labeling the outer leaflet of CHO-K1 cell membranes. J: Autocorrelation curves for TopFluor-PC labeling the inner leaflet of CHO-K1 cell membranes. K: FCS diffusion law plots for TopFluor-PC diffusion in the outer and inner leaflets of CHO-K1 cell membranes. L: Autocorrelation curves for TopFluor-PC labeling the outer leaflet of RBL-2H3 cell membranes. M: Autocorrelation curves for TopFluor-PC labeling the inner leaflet of RBL-2H3 cell membranes. N: FCS diffusion law plots for TopFluor-PC diffusion in the outer and inner leaflets of RBL-2H3 cell membranes. A comparison of absolute fluorescence decay traces and a fluorescence lifetime histogram of labeled samples with unlabeled samples are shown in supplemental Fig. S4.

probes are sensitive to cholesterol content we performed mβcd-induced cholesterol-depletion experiments. We observed that, as expected, cholesterol depletion significantly affected the NBD-SM lifetime, as indicated by a drop of 6 ns in both cell lines (supplemental Fig. S6). However, the NBD-PC lifetime showed a decline of only 1 ns. This experiment verifies that the disruption of cholesterol domains directly influences the SM microenvironment but to a

much lesser extent that of PC. Thus, NBD lipid analogs reside in environments similar to their endogenous forms and therefore can be used to examine the domain-specific plasma membrane organization.

Next, we proceeded with the leaflet-specific analysis of SM probes. The lifetime analysis of NBD-SM immediately after labeling (i.e., in the outer leaflet) shows a lifetime of ~10.5 ns in both cell lines (**Fig. 4A**, B, **Fig. 5A**–H), suggesting the existence of ordered domains surrounding the NBD-SM molecules in the outer leaflet. ITIR-FCS results show that in the case of TF-SM, D in the outer leaflet is ~2-fold higher in CHO-K1 (0.45 ± 0.07 $\mu m^2/s$) than in RBL-2H3 (0.22 ± 0.03 $\mu m^2/s$) cells (Figs. 4C, D, 5I–N). As expected, the τ_0 was positive in the outer leaflet of both cells, with a higher value in RBL-2H3 (τ_0 = 1.25 ± 0.25 s) than in CHO-K1 (τ_0 = 0.59 ± 0.12 s) cells, consistent with the existence of a fraction of l_o phase in the outer leaflet. After the transbilayer redistribution of the probe between both leaflets (Fig. 1B, middle), the lifetime of NBD-SM was 0.5 ns shorter than in the outer leaflet of CHO-K1 cells. However, in RBL-2H3 cells there was a 1 ns increase in the lifetime of the probe, implying that postredistribution NBD-SM localizes in more ordered microenvironments. ITIR-FCS measurements showed a 40% increase of D and a drop of τ_0 for TF-SM in CHO-K1 cells, suggesting faster lipid mobility in the inner leaflet, while in RBL-2H3 cells there was no significant difference in the lipid mobility and probe entrapment. The subsequent analysis of NBD-SM exclusively on the inner leaflet confirmed the existence of an l_d phase in the inner leaflet of CHO-K1 cells, as shown by a fluorescence lifetime of 7.80 ± 0.55 ns and an even more ordered inner leaflet in RBL-2H3 cells (lifetime of 9.1 ± 0.04 ns). The fraction of the long lifetime in the inner leaflet was reduced to ~30% with respect to 50% in the outer leaflet for both cell lines. Consistent with lifetime measurements, TF-SM showed a 36% higher D in the inner leaflet relative to that in the outer leaflet, and τ_0 was reduced from 0.59 ± 0.12 to 0.38 ± 0.13 s in the inner leaflet of CHO-K1 cells. On the contrary, a comparison of inner and outer leaflets revealed that there was no significant difference in D in RBL-2H3 cells. Moreover, the change in τ_0 showed no significant effect (1.25 ± 0.25 to 1.08 ± 0.23 s), as indicated by a t-test ($P < 0.05$). In contrast to PC, SM lipid analogs in RBL-2H3 cells indicated a higher domain fraction in the inner leaflet of the plasma membrane, leading to slow diffusion and a longer lifetime.

Our results reveal differences in individual leaflet packing in the two cell lines. CHO-K1 cells show a more profound difference between the outer and inner leaflet environment than RBL-2H3 cells. This could imply the occurrence of higher dynamic coupling between the two leaflets in RBL-2H3 cells. Unlike PC analogs, SM analogs manifest similar dynamics and organization when compared between the two leaflets. Previous studies suggest that interdigitation of SM can mediate interleaflet coupling in the plasma membrane (54). Similar dynamics of SM probes in the two leaflets could support the proposition of SM-mediated interleaflet coupling. Furthermore, our readouts obtained on SM probes also show that RBL-2H3 cells manifest a more ordered membrane environment than CHO-K1 cells, as already noted in the case of PC analogs.

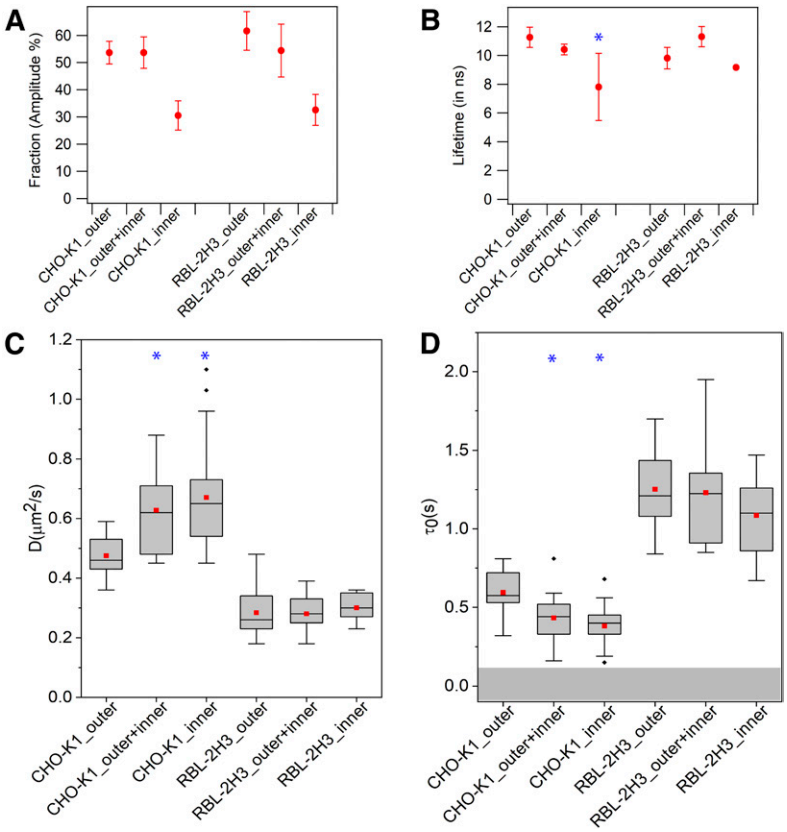

Fig. 4. Leaflet-specific FLIM and ITIR-FCS analysis of fluorescently labeled SM analogs in CHO-K1 and RBL-2H3 cells at room temperature. A: Fraction percentage (amplitude) of NBD-SM long lifetime. B: Long lifetime of NBD-SM measured in nanoseconds. Only the long lifetime is shown (see legend to Fig. 2). C: Average diffusion coefficient of TopFluor-SM. D: FCS diffusion law intercept of TopFluor-SM. Data are pooled averages, and error bars are SDs. ITIR-FCS data are represented as means of boxplots. Maximum and minimum values are shown as vertical boxes with error bars; the 1st and 99th percentiles are shown. Means are shown as red squares. To ensure reproducibility, FLIM experiments were repeated at least three times independently. ITIR-FCS data are the averages of at least 12 measurements, each done on different cells from three independent experiments. *Significant differences with respect to the values measured in the outer leaflet (paired t-test; $P < 0.05$).

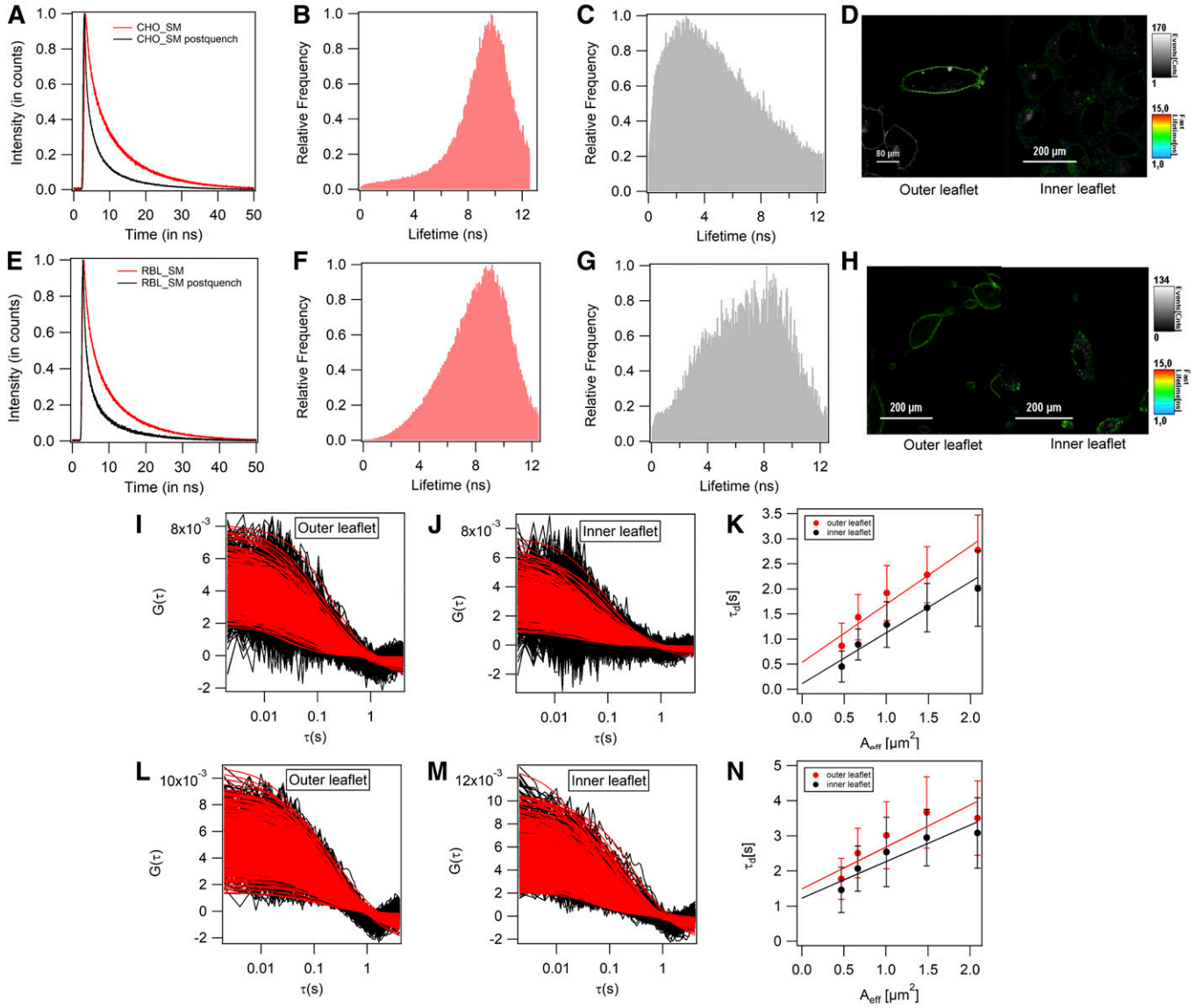

Fig. 5. Representative raw data for FLIM and ITIR-FCS experiments for analyzing leaflet-specific dynamics and organization of SM fluorescent analogs. A: Normalized averaged intensity decay of NBD-SM in the outer and inner leaflets of CHO-K1 cell membranes. B: Normalized lifetime histogram of NBD-SM in the outer leaflet of CHO-K1 cell membranes. C: Normalized lifetime histogram of NBD-SM in the inner leaflet of CHO-K1 cell membranes. D: Lifetime map of CHO-K1 cells labeled with NBD-SM. E: Normalized averaged intensity decay of NBD-SM in the outer and inner leaflets of RBL-2H3 cell membranes. F: Normalized lifetime histogram of NBD-SM in the outer leaflet of RBL-2H3 cell membranes. G: Normalized lifetime histogram of NBD-SM in the inner leaflet of RBL-2H3 cell membranes. H: Lifetime map of RBL-2H3 cells labeled with NBD-SM. I: Autocorrelation curves for TopFluor-SM labeling the outer leaflet of CHO-K1 cell membranes. J: Autocorrelation curves for TopFluor-SM labeling the inner leaflet of CHO-K1 cell membranes. K: FCS diffusion law plots for TopFluor-SM diffusion in the outer and inner leaflets of CHO-K1 cell membranes. L: Autocorrelation curves for TopFluor-SM labeling the outer leaflet of RBL-2H3 cell membranes. M: Autocorrelation curves for TopFluor-SM labeling the inner leaflet of RBL-2H3 cell membranes. N: FCS diffusion law plots for TopFluor-SM diffusion in the outer and inner leaflets of RBL-2H3 cell membranes. A comparison of absolute fluorescence decay traces and a fluorescence lifetime histogram of labeled samples with unlabeled samples are shown in supplemental Fig. S4.

In summary, in addition to demonstrating a lower degree of heterogeneity in the inner leaflet, our results demonstrate that the asymmetric arrangement of the plasma membrane can vary for different cell lines used. Furthermore, probe-related differences suggest that different aspects of organization and dynamics are recorded. This can be visualized by analyzing the differences in the ratios of D measured in the inner leaflet and the outer leaflet, which also demonstrate the probe and cell line-specific plasma membrane asymmetry (supplemental Table S2).

Leaflet-specific analysis of PS fluorescent analogs in CHO-K1 and RBL-2H3 cell membranes

We probed the organization and dynamics of fluorescent PS analogs to characterize the inner leaflet organization (55). Usually, it comprises the fluid fraction of the plasma membrane (56); however, there is evidence suggesting its direct interaction with the cytoskeleton, due to which PS can exhibit lower mobility (57). Close proximity of the inner leaflet with the cytoskeletal network could also alter the mode of lipid diffusion, as molecules hindered by

meshworks are shown to undergo hop diffusion (58), and additional protein interactions in the inner leaflet could result in distinct lipid microenvironments (59).

First, we estimated the percentage of PS probes residing in the inner leaflet by performing outer leaflet fluorescence quenching experiments. In CHO-K1 cells, ~70% PS fluorescent analogs resided in the inner leaflet, while in RBL-2H3 cells 80% of probe molecules were in the inner leaflet (supplemental Table S1).

When measured in the outer leaflet, NBD-PS showed a lifetime of 10.21 ± 0.62 ns in CHO-K1 cells and 8.98 ± 0.29 ns in RBL-2H3 cells (**Fig. 6A**, B, **Fig. 7A**–H), indicating the existence of an l_o phase in the outer leaflet. Unlike PC and SM analogs, in which the occurrence of an l_o phase correlated with slower lipid mobility, TF-PS diffused 2-fold faster and showed lower transient entrapment than the TF-PC and TF-SM in the respective cell lines measured under the same experimental conditions (Figs. 6C, D, 7I–N). In this case as well, the *D* of TF-PS was ~2.5 times higher in CHO-K1 cells (1.1 ± 0.26 $\mu m^2/s$) than in RBL-2H3 cells (0.47 ± 0.13 $\mu m^2/s$). Moreover, transient entrapment of the probe in domains was significantly lower in CHO-K1 cells (τ_0 = 0.27 ± 0.12 s) than in RBL-2H3 cells (τ_0 = 0.81 ± 0.19 s). A combined readout from the two leaflets showed a 2 ns drop of the NBD-PS lifetime in CHO-K1 cells, but no significant change was observed in RBL-2H3 cells. However, the TF-PS dynamics remained largely unaltered for both cell lines when the two leaflets were analyzed together. Finally, on probing the inner leaflet exclusively, we observed a 2.3 ns lower lifetime of NBD-PS in the CHO-K1 inner leaflet relative to the outer leaflet, while it remained the same in RBL-2H3 cells. Moreover, the fraction of the long lifetime component originating from NBD-PS was reduced to 30% in both cell lines. Consistent with this trend, a lowering of the NBD-PS lifetime was accompanied with a 26% faster diffusion of TF-PS and τ_0 close to the threshold for free diffusion in CHO-K1 cells. Despite the same lifetime in RBL-2H3 cells, we observed a 120% higher *D* (0.47 ± 0.13 to 1.08 ± 0.23 $\mu m^2/s$) in the inner leaflet of the membrane and τ_0 decline from 0.73 ± 0.19 s in the outer leaflet to 0.22 ± 0.08 s in the inner leaflet. This could mean that the differences in the microenvironment of NBD-PS in the two leaflets of RBL-2H3 cell membranes were below the detection limits of FLIM. NBD-PS and NBD-PC lifetime has also been measured to be similar in HeLa cells (16). In this regard, it is important to consider that in addition to membrane packing, NBD lifetime is sensitive to environmental polarity. Moreover, NBD probes have been shown to exhibit red-edge excitation shift when NBD lipid probes loop back at the water-membrane interface (25, 60). Due to the multiple factors that influence the NBD lifetime, an evaluation of NBD lifetime alone can result in misleading interpretations, and it is essential to supplement the lifetime results with another quantitative method such as ITIR-FCS, as used in this study.

These observations indicate an overall higher molecular mobility of PS lipid analogs in cell membranes compared with other choline lipids. In CHO-K1 cells, PS lipid analogs show a distinct microenvironment in the two leaflets, as assessed by the NBD lifetime and TF-PS diffusion.

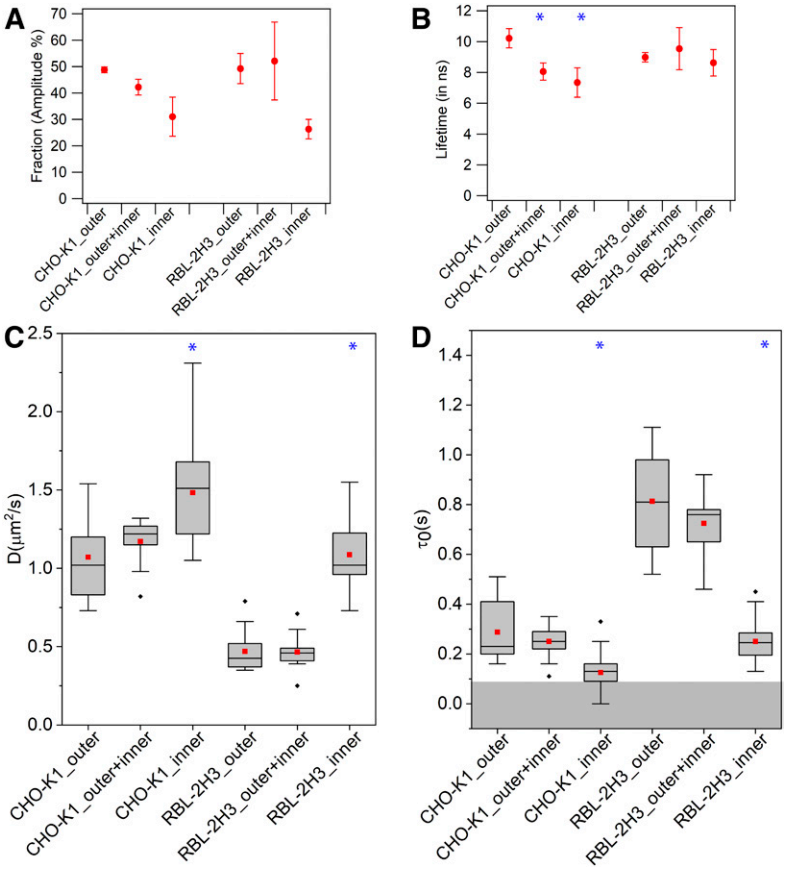

Fig. 6. Leaflet-specific FLIM and ITIR-FCS analysis of fluorescently labeled PS analogs in CHO-K1 and RBL-2H3 cells at room temperature. A: Fraction percentage (amplitude) of NBD-PS long lifetime. B: Long lifetime of NBD-PS measured in nanoseconds. Only the long lifetime is shown (see legend to Fig. 2). C: Average diffusion coefficient of TopFluor-PS. D: FCS diffusion law intercept of TopFluor-PS. Data are pooled averages, and error bars are SDs. To ensure reproducibility, FLIM experiments were repeated at least three times independently. ITIR-FCS data are represented as means of boxplots. Maximum and minimum values are shown as vertical boxes with error bars; the 1st and 99th percentiles are shown. Means are shown as red squares. ITIR-FCS data are the averages of at least 12 measurements, each done on different cells from three independent experiments. *Significant differences with respect to the values measured in the outer leaflet (paired *t*-test; $P < 0.05$).

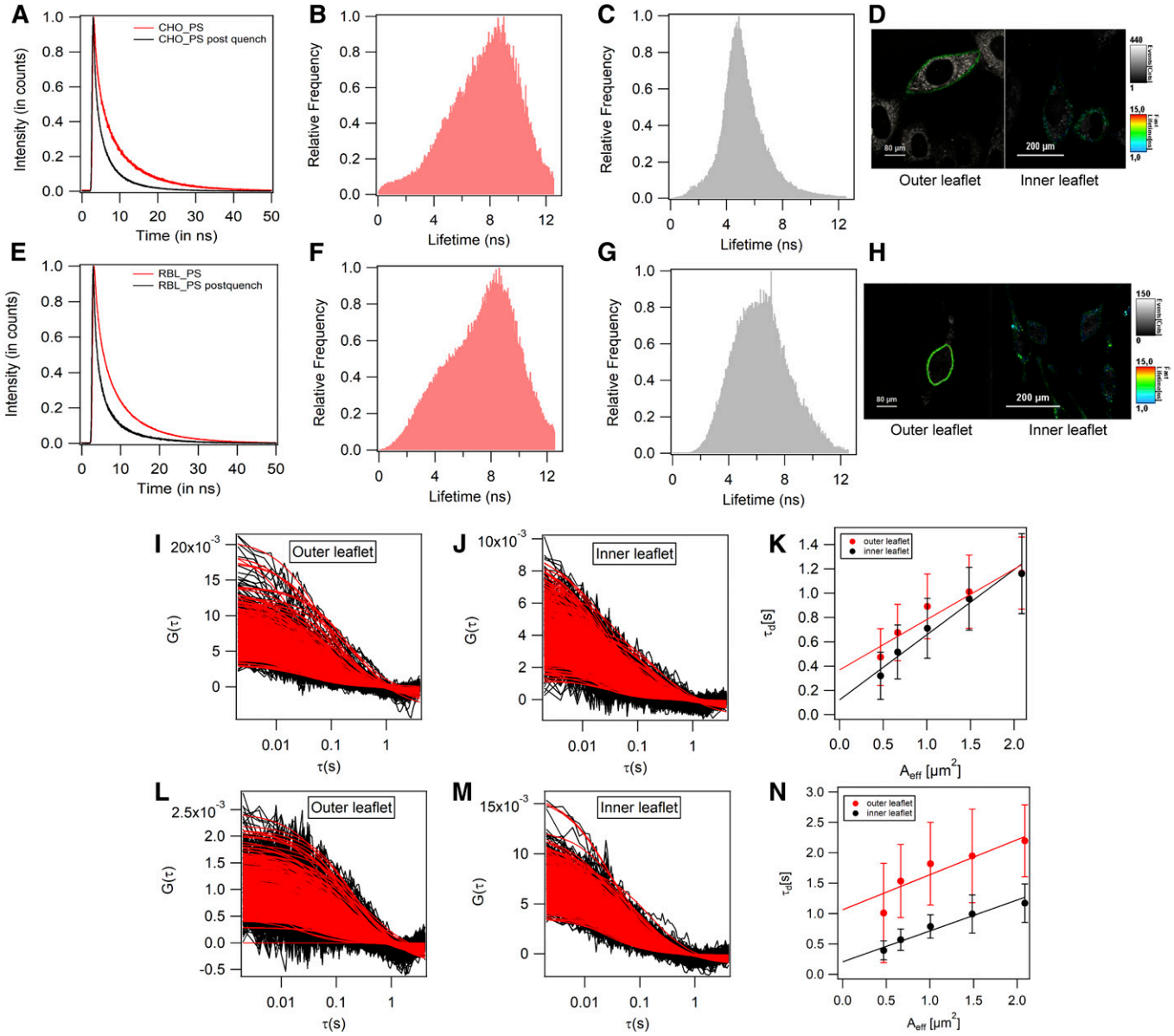

Fig. 7. Representative raw data for FLIM and ITIR-FCS experiments for analyzing leaflet-specific dynamics and organization of PS fluorescent analogs. A: Normalized averaged intensity decay of NBD-PS in the outer and inner leaflets of CHO-K1 cell membranes. B: Normalized lifetime histogram of NBD-PS in the outer leaflet of CHO-K1 cell membranes. C: Normalized lifetime histogram of NBD-PS in the inner leaflet of CHO-K1 cell membranes. D: Lifetime map of CHO-K1 cells labeled with NBD-PS. E: Normalized averaged intensity decay of NBD-PS in the outer and inner leaflets of RBL-2H3 cell membranes. F: Normalized lifetime histogram of NBD-PS in the outer leaflet of RBL-2H3 cell membranes. G: Normalized lifetime histogram of NBD-PS in the inner leaflet of RBL-2H3 cell membranes. H: Lifetime map of RBL-2H3 cells labeled with NBD-PS. I: Autocorrelation curves for TopFluor-PS labeling the outer leaflet of CHO-K1 cell membranes. J: Autocorrelation curves for TopFluor-PS labeling the inner leaflet of CHO-K1 cell membranes. K: FCS diffusion law plots for TopFluor-PS diffusion in the outer and inner leaflets of CHO-K1 cell membranes. L: Autocorrelation curves for TopFluor-PS labeling the outer leaflet of RBL-2H3 cell membranes. M: Autocorrelation curves for TopFluor-PS labeling the inner leaflet of RBL-2H3 cell membranes. N: FCS diffusion law plots for TopFluor-PS diffusion in the outer and inner leaflets of RBL-2H3 cell membranes. A comparison of absolute fluorescence decay traces and a fluorescence lifetime histogram of labeled samples with unlabeled samples are shown in supplemental Fig. S4.

Moreover, while in the inner leaflet PS lipid analogs reside in a more fluid environment, as revealed by lifetime characteristics of l_d-phase vesicles (DOPC), higher mobility, and free diffusion of the probe. RBL-2H3 cells, on the other hand, do not show differences in NBD-PS environment in the two leaflets. However, significant differences in the diffusion properties of TF-PS in the two leaflets suggest a less viscous environment in the inner leaflet (61). Despite the lower membrane viscosity, factors such as cytoskeleton network and protein interactions could alter the solvent polarity and tendency of NBD probes to loop back, which can contribute to the long NBD lifetimes in the inner leaflet. The composite membrane model proposed by Gowrishankar et al. (62) suggests the formation of nanoclusters in the membrane upon actin cytoskeleton binding. However, our results indicate that PS probes are located in a fluid

environment with minimal domain entrapment. This discrepancy could be due to the variation in the affinity of inner leaflet components for the actin cytoskeleton. For instance, PMT-GFP, an inner membrane marker known to interact with the actin cytoskeleton (41), shows a diffusion coefficient comparable to that of PC lipid analogs (supplemental Fig. S2). It again suggests probe-specific readouts of dynamics and organization. Therefore, for a clearer idea regarding the plasma membrane dynamics, it is important to examine more than one type of lipids. However, as PS is one of the most abundant inner leaflet lipids of mammalian cells, the observation of a more fluid membrane environment with PS probes can describe the inner leaflet dynamics and organization in general.

General discussion

Plasma membrane asymmetry and dynamic coupling of the two membrane leaflets are among the most challenging open questions in membrane biology. The two most prominent propositions in the literature that describe the interleaflet communication are domain texturing on the outer leaflet and dynamically fluctuating molecular heterogeneity. According to the outer leaflet domain-texturing idea, membrane phase changes leading to domain formation in the outer leaflet are transmitted to the inner leaflet of the membrane, influencing its organization (63). In other words, this model supports the existence of dynamic coupling between the leaflets. There are reports suggesting dynamic fluctuations of membrane heterogeneity, resulting in temporal changes in the diffusivities of membrane components (59). When measured at long time scales (milliseconds), constant dynamic fluctuations in the membrane could appear as weak dynamic coupling between the leaflets. Our results on SM probes in RBL-2H3 cells do provide evidence for interleaflet transmission of domain texturing to the inner leaflet; however, PC and PS probes do not show this transmission. It is important to note that despite high spatial and temporal resolutions, FLIM and ITIR-FCS still suffer from certain limitations that might hinder the observation of fluctuating nanodomains. For instance, due to long measurement times, FLIM is incapable of recording short molecular fluctuations. In addition, a simulation-based study suggested that domain movements can influence the diffusion law plot (64). If small domains show low affinity for the probe or are mobile but are diffusing with a diffusion coefficient comparable to lipid diffusion, then diffusion law will be unable to detect them.

CONCLUSIONS

The plasma membrane is structurally complex and dynamic with a diversity of lateral molecular movements ranging from directed diffusion of immobile protein-lipid clusters to free diffusion of molecules and transversal movements of lipids occurring at varying rates. In addition, there are fluctuating nanoscale assemblies on the membrane scaling from 5 to 500 nm. To understand the organization and dynamics of such a system, it is essential to use methods with varying spatial and temporal resolutions. In this study, we performed a spatiotemporal analysis of the plasma membrane asymmetry in live mammalian cells using advanced fluorescence methods with multiplexing capabilities, namely FLIM and ITIR-FCS. These methodologies enabled us to distinguish domain- and leaflet-specific organization and dynamics, even across closely related cell lines. We characterized the plasma membrane asymmetry by evaluating the microenvironment and dynamics of fluorescent analogs of PC, SM, and PS, which exhibit specific preferences for domains and leaflets.

By using a combinatorial approach of FLIM and ITIR-FCS, we can sense the microenvironment independent of concentration and mobility (FLIM) while at the same time measuring membrane dynamics and organization (ITIR-FCS). Our results show that in general in mammalian cell membranes, the outer leaflet is more densely packed than the inner leaflet, as demonstrated by a longer lifetime, slower probe mobility, and greater transient confinement of lipids (Figs. 2–7) in the former than the latter. However, the detailed membrane dynamics and organization reveals cell line-specific differences in the plasma membrane asymmetry. For instance, in RBL-2H3 cells, SM analogs showed similar membrane packing and diffusion properties in both leaflets (Fig. 4), while in CHO-K1 cells clear differences for SM analogs were detected between both leaflets, possibly implying strong interleaflet coupling in RBL cells. Furthermore, accessible details of membrane dynamics and organization depend also on the probes used, as shown by probe-specific readouts.

Overall, our study demonstrates how FLIM and ITIR-FCS can analyze differences in dynamics and organization between outer and inner plasma membrane leaflets, as seen by different probe molecules independent of the cell line investigated.

REFERENCES

1. Kusumi, A., K. G. N. Suzuki, R. S. Kasai, K. Ritchie, and T. K. Fujiwara. 2011. Hierarchical mesoscale domain organization of the plasma membrane. *Trends Biochem. Sci.* **36:** 604–615.
2. Kusumi, A., T. K. Fujiwara, R. Chadda, M. Xie, T. A. Tsunoyama, Z. Kalay, R. S. Kasai, and K. G. Suzuki. 2012. Dynamic organizing principles of the plasma membrane that regulate signal transduction: commemorating the fortieth anniversary of Singer and Nicolson's fluid-mosaic model. *Annu. Rev. Cell Dev. Biol.* **28:** 215–250.
3. Meder, D., M. J. Moreno, P. Verkade, W. L. C. Vaz, and K. Simons. 2006. Phase coexistence and connectivity in the apical membrane of polarized epithelial cells. *Proc. Natl. Acad. Sci. USA.* **103:** 329–334.
4. Fujimoto, T., and I. Parmryd. 2017. Interleaflet coupling, pinning, and leaflet asymmetry—major players in plasma membrane nanodomain formation. *Front. Cell Dev. Biol.* **4:** 155.
5. Devaux, P. F. 1991. Static and dynamic lipid asymmetry in cell membranes. *Biochemistry.* **30:** 1163–1173.
6. van Meer, G. 2011. Dynamic transbilayer lipid asymmetry. **3:** a004671.
7. Andrews, N. L., K. A. Lidke, J. R. Pfeiffer, A. R. Burns, B. S. Wilson, J. M. Oliver, and D. S. Lidke. 2008. Actin restricts FcεRI diffusion and facilitates antigen-induced receptor immobilisation. *Nat. Cell Biol.* **10:** 955–963.
8. Fadok, V. A., D. R. Voelker, P. A. Campbell, J. J. Cohen, D. L. Bratton, and P. M. Henson. 1992. Exposure of phosphatidylserine on the surface of apoptotic lymphocytes triggers specific recognition and removal by macrophages. J. Immunol. **148:** 2207–2216.

9. Kasson, P. M., and V. S. Pande. 2007. Control of membrane fusion mechanism by lipid composition: predictions from ensemble molecular dynamics. *PLOS Comput. Biol.* **3:** e220.
10. O'Donnell, V. B., J. Rossjohn, and M. J. Wakelam. 2018. Phospholipid signaling in innate immune cells. *J. Clin. Invest.* **128:** 2207–2216.
11. van Meer, G., D. R. Voelker, and G. W. Feigenson. 2008. Membrane lipids: where they are and how they behave. *Nat. Rev. Mol. Cell Biol.* **9:** 112–124.
12. Róg, T., A. Orłowski, A. Llorente, T. Skotland, T. Sylvänne, D. Kauhanen, K. Ekroos, K. Sandvig, and I. Vattulainen. 2016. Interdigitation of long-chain sphingomyelin induces coupling of membrane leaflets in a cholesterol dependent manner. *Biochim. Biophys. Acta.* **1858:** 281–288.
13. Son, M., and E. London. 2013. The dependence of lipid asymmetry upon phosphatidylcholine acyl chain structure. **54:** 223–231.
14. Lin, W., C. D. Blanchette, T. V. Ratto, and M. L. Longo. 2006. Lipid asymmetry in DLPC/DSPC-supported lipid bilayers: a combined AFM and fluorescence microscopy study. **90:** 228–237.
15. Devaux, P. F., and A. Herrmann. 2011. Transmembrane Dynamics of Lipids. Wiley, New York.
16. Stöckl, M., A. P. Plazzo, T. Korte, and A. Herrmann. 2008. Detection of lipid domains in model and cell membranes by lipid analogues. *J. Biol. Chem.* **283:** 30828–30837.
17. Schröter, F., U. Jakop, A. Teichmann, I. Haralampiev, A. Tannert, B. Wiesner, P. Müller, and K. Müller. 2016. Lipid dynamics in boar sperm studied by advanced fluorescence imaging techniques. **45:** 149–163.
18. Bag, N., S. Huang, and T. Wohland. 2015. Plasma membrane organization of epidermal growth factor receptor in resting and ligand-bound states. *Biophys. J.* **109:** 1925–1936.
19. Bag, N., J. Sankaran, A. Paul, R. S. Kraut, and T. Wohland. 2012. Calibration and limits of camera-based fluorescence correlation spectroscopy: a supported lipid bilayer study. *ChemPhysChem.* **13:** 2784–2794.
20. Krieger, J. W., A. P. Singh, N. Bag, C. S. Garbe, T. E. Saunders, J. Langowski, and T. Wohland. 2015. Imaging fluorescence (cross-) correlation spectroscopy in live cells and organisms. *Nat. Protoc.* **10:** 1948–1974.
21. Gupta, A., J. K. Marzinek, D. Jefferies, P. J. Bond, P. Harryson, and T. Wohland. 2019. The disordered plant dehydrin Lti30 protects the membrane during water-related stress by cross-linking lipids. *J. Biol. Chem.* **294:** 6468–6482.
22. Wawrezinieck, L., H. Rigneault, D. Marguet, and P. F. Lenne. 2005. Fluorescence correlation spectroscopy diffusion laws to probe the submicron cell membrane organization. *Biophys. J.* **89:** 4029–4042.
23. Ng, X. W., N. Bag, and T. Wohland. 2015. Characterization of lipid and cell membrane organization by the fluorescence correlation spectroscopy diffusion law. *Chimia (Aarau).* **69:** 112–119.
24. Chapman. C. F., Y. Liu, G. J. Sonek, and B. J. Tromberg. 1995. The use of exogeneous fluorescent probes for temperature measurements in single living cells. *Photochem. Photobiol.* **62:** 416–425.
25. Raghuraman, H., S. Shrivastava, and A. Chattopadhyay. 2007. Monitoring the looping up of acyl chain labeled NBD lipids in membranes as a function of membrane phase state. *Biochim. Biophys. Acta.* **1768:** 1258–1267.
26. Stöckl, M. T., and A. Herrmann. 2010. Detection of lipid domains in model and cell membranes by fluorescence lifetime imaging microscopy. *Biochim. Biophys. Acta.* **1798:** 1444–1456.
27. Sezgin, E., F. B. Can, F. Schneider, M. P. Clausen. S. Galiani, T. A. Stanly, D. Waithe, A. Colaco, A. Honigmann, D. Wüstner, et al. 2016. A comparative study on fluorescent cholesterol analogs as versatile cellular reporters. *J. Lipid Res.* **57:** 299–309.
28. Kay, J. G., M. Koivusalo, X. Ma, T. Wohland, and S. Grinstein. 2012. Phosphatidylserine dynamics in cellular membranes. *Mol. Biol. Cell.* **23:** 2198–2212.
29. Sezgin, E., H-J. Kaiser, T. Baumgart, P. Schwille, K. Simons, and I. Levental. 2012. Elucidating membrane structure and protein behavior using giant plasma membrane vesicles. *Nat. Protoc.* **7:** 1042–1051.
30. Sankaran, J., X. Shi, L. Y. Ho, E. H. K. Stelzer, and T. Wohland. 2010. ImFCS: a software for imaging FCS data analysis and visualization. *Opt. Express.* **18:** 25468–25481.
31. Holthuis, J. C. M., and T. P. Levine. 2005. Lipid traffic: floppy drives and a superhighway. *Nat. Rev. Mol. Cell Biol.* **6:** 209–220.
32. Pomorski, T., P. Müller, B. Zimmermann, K. Burger, P. F. Devaux, and A. Herrmann. 1996. Transbilayer movement of fluorescent and spin-labeled phospholipids in the plasma membrane of human fibroblasts: a quantitative approach. *J. Cell Sci.* **109:** 687–698.
33. Pomorski, T., A. Herrmann, A. Zachowski, P. F. Devaux, and P. Müllery. 1994. Rapid determination of the transbilayer distribution of NBD-phospholipids in erythrocyte membranes with dithionite. *Mol. Membr. Biol.* **11:** 39–44.
34. Daleke, D. L. 2003. Regulation of transbilayer plasma membrane phospholipid asymmetry. *J. Lipid Res.* **44:** 233–242.
35. Chapple, J. P., A. J. Hardcastle, C. Grayson, L. A. Spackman, K. R. Willison, and M. E. Cheetham. 2000. Mutations in the N-terminus of the X-linked retinitis pigmentosa protein RP2 interfere with the normal targeting of the protein to the plasma membrane. *Hum. Mol. Genet.* **9:** 1919–1926.
36. Chapple, J. P., C. Grayson, K. Willison, A. Hardcastle, and M. Cheetham. 2002. Delineation of the plasma membrane targeting domain of RP2. *Invest. Ophthalmol. Vis. Sci.* **43:** 2015–2020.
37. Veerapathiran, S., and T. Wohland. 2018. The imaging FCS diffusion law in the presence of multiple diffusive modes. *Methods.* **140-141:** 140–150.
38. Veatch, S. L., and S. L. Keller. 2003. A closer look at the canonical "raft mixture" in model membrane studies. *Biophys. J.* **84:** 725–726.
39. Veatch, S. L., and S. L. Keller. 2003. Separation of liquid phases in giant vesicles of ternary mixtures of phospholipids and cholesterol. *Biophys. J.* **85:** 3074–3083.
40. Gupta, A., S. Muralidharan, F. Torta, and M. R. Wenk. 2019. Long acyl chain ceramides govern cholesterol and cytoskeleton dependence of membrane outer leaflet dynamics. *bioRxiv* .
41. Huang, S., S. Y. Lim, A. Gupta, N. Bag, and T. Wohland. 2017. Plasma membrane organization and dynamics is probe and cell line dependent. *Biochim. Biophys. Acta.* **1859:** 1483–1492.
42. Bag, N., D. H. X. Yap, and T. Wohland. 2014. Temperature dependence of diffusion in model and live cell membranes characterized by imaging fluorescence correlation spectroscopy. *Biochim. Biophys. Acta.* **1838:** 802–813.
43. Kraft, M. L. 2017. Sphingolipid organization in the plasma membrane and the mechanisms that influence it. *Front. Cell Dev. Biol.* **4:** 154.
44. Schneider, F., D. Waithe, M. P. Clausen, S. Galiani, T. Koller, G. Ozhan, M. P. Clausen, C. Eggeling, and Sezgin, E. 2017. Diffusion of lipids and GPI-anchored proteins in actin-free plasma membrane vesicles measured by STED-FCS. *Mol. Biol. Cell.* **28:** 1507–1518.
45. Endapally, S., D. Frias, M. Grzemska, A. Gay, D. R. Tomchick, and A. Radhakrishnan. 2019. Molecular discrimination between two conformations of sphingomyelin in plasma article molecular discrimination between two conformations of sphingomyelin in plasma membranes. *Cell.* **176:** 1040–1053.e17.
46. Simons, K., and W. L. Vaz. 2004. Model systems, lipid rafts, and cell membranes. *Annu. Rev. Biophys. Biomol. Struct.* **33:** 269–295.
47. Simons, K., and E. Ikonen. 1997. Functional rafts in cell membranes. *Nature.* **387:** 569–572.
48. Lingwood, D., H-J. Kaiser, I. Levental, and K. Simons. 2009. Lipid rafts as functional heterogeneity in cell membranes. *Biochem. Soc. Trans.* **37:** 955–960.
49. Lingwood, D., and K. Simons. 2010. Lipid rafts as a membrane-organizing principle. *Science.* **327:** 46–50.
50. Zhang, P., B. Liu, G. M. Jenkins, Y. A. Hannun, and L. M. Obeid. 1997. Expression of neutral sphingomyelinase identifies a distinct pool of sphingomyelin involved in apoptosis. *J. Biol. Chem.* **272:** 9609–9612.
51. Linardic, C. M., and Y. A. Hannuns. 1994. Identification of a distinct pool of sphingomyelin involved in the sphingomyelin cycle. *J. Biol. Chem.* **269:** 23530–23537.
52. Mukherjee, S., X. Zha, I. Tabas, and F. R. Maxfield. 1998. Cholesterol distribution in living cells: fluorescence imaging using dehydroergosterol as a fluorescent cholesterol analog. *Biophys. J.* **75:** 1915–1925.
53. Scheidt, H. A., P. Mu, A. Herrmann, and D. Huster. 2003. The potential of fluorescent and spin-labeled steroid analogs to mimic natural cholesterol. *J. Biol. Chem.* **278:** 45563–45569.
54. Raghupathy, R., A. A. Anilkumar, A. Polley, P. P. Singh, M. Yadav, C. Johnson, S. Suryawanshi, V. Saikam, S. D. Sawant, A. Panda, et al. 2015. Transbilayer lipid interactions mediate nanoclustering of lipid-anchored proteins. *Cell.* **161:** 581–594.
55. Daleke, D. L. 2007. Phospholipid flippases. *J. Biol. Chem.* **282:** 821–825.
56. Wang, T. Y., and J. R. Silvius. 2001. Cholesterol does not induce segregation of liquid-ordered domains in bilayers modeling the inner leaflet of the plasma membrane. *Biophys. J.* **81:** 2762–2773.
57. An, X., X. Guo, H. Sum, J. Morrow, W. Gratzer, and N. Mohandas. 2004. Phosphatidylserine binding sites in erythroid spectrin: location and implications for membrane stability. *Biochemistry.* **43:** 310–315.

58. Marguet, D., P. F. Lenne. H. Rigneault, and H. T. He. 2006. Dynamics in the plasma membrane: how to combine fluidity and order. *EMBO J.* **25:** 3446–3457.
59. Yamamoto, E., T. Akimoto, A. C. Kalli, K. Yasuoka, and M. S. P. Sansom. 2017. Dynamic interactions between a membrane binding protein and lipids induce fluctuating diffusivity. *Sci. Adv.* **3:** e1601871.
60. Amaro, M., H. A. L. Filipe, J. P. Prates Ramalho, M. Hof, and L. M. S. Loura. 2016. Fluorescence of nitrobenzoxadiazole (NBD)-labeled lipids in model membranes is connected not to lipid mobility but to probe location. *Phys. Chem. Chem. Phys.* **18:** 7042–7054.
61. Morrot, G., S. Cribier, P. F. Devaux, D. Geldwerth, J. Davoust, J. F. Bureau, P. Fellmann, P. Herve, and B. Frilley.1986. Asymmetric lateral mobility of phospholipids in the human erythrocyte membrane. *Proc. Natl. Acad. Sci. USA.* **83:** 6863–6867.
62. Gowrishankar, K., S. Ghosh, S. Saha, C. Rumamol, S. Mayor, and M. Rao. 2012. Theory active remodeling of cortical actin regulates spatiotemporal organization of cell surface molecules. *Cell.* **149:** 1353–1367.
63. Watkins, E. B., C. E. Miller, J. Majewski, and T. L. Kuhl. 2011. Membrane texture induced by specific protein binding and receptor clustering: active roles for lipids in cellular function. *Proc. Natl. Acad. Sci. USA.* **108:** 6975–6980.
64. Šachl, R., J. Bergstrand, J. Widengren, and M. Hof. 2016. Fluorescence correlation spectroscopy diffusion laws in the presence of moving nanodomains. *J. Phys. D Appl. Phys.* **49:** 114002.